# Optothermally induced mechanical oscillation in a silk fibroin coated high-Q microsphere

Cite as: Appl. Phys. Lett. **116**, 201104 (2020); https://doi.org/10.1063/1.5142649 Submitted: 17 December 2019 . Accepted: 08 May 2020 . Published Online: 18 May 2020

Yiming Liu, Xuefeng Jiang, Changqing Wang, and Lan Yang 🗓







# ARTICLES YOU MAY BE INTERESTED IN

Spinwave detection by nitrogen-vacancy centers in diamond as a function of probe-sample separation

Applied Physics Letters 116, 202401 (2020); https://doi.org/10.1063/1.5141921

Narrow linewidth characteristics of interband cascade lasers
Applied Physics Letters 116, 201101 (2020); https://doi.org/10.1063/5.0006823

Flexible measurement of high-order optical orbital angular momentum with a variable cylindrical lens pair

Applied Physics Letters 116, 201105 (2020); https://doi.org/10.1063/5.0002756

Lock-in Amplifiers up to 600 MHz







# Optothermally induced mechanical oscillation in a silk fibroin coated high-Q microsphere

Cite as: Appl. Phys. Lett. **116**, 201104 (2020); doi: 10.1063/1.5142649 Submitted: 17 December 2019 · Accepted: 8 May 2020 ·

Published Online: 18 May 2020







Yiming Liu, Xuefeng Jiang, Changqing Wang, and Lan Yang<sup>a)</sup> 🕞

# AFFILIATIONS

Electrical and Systems Engineering Department, Washington University, St. Louis, Missouri 63130, USA

a) Author to whom correspondence should be addressed: yang@seas.wustl.edu

### **ABSTRACT**

Protein-based optical devices with biocompatibility and biodegradability have distinct advantages for applications in biomedical sensing. Silk fibroin with unique optical, thermal, and mechanical properties renders great flexibility in designing functional photonic platforms. Here, we report the experimental observation of optothermally induced mechanical oscillation in a silk-fibroin coated microcavity. Theoretical analysis reveals that the observed oscillation results from the interplay of several nonlinear effects in the silk-coated-microsphere as well as the coexistence of fast and slow thermal dynamic processes. The physics in our study breaks ground for the study of nonlinear dynamics of structural protein optical material that can be used for functional optical devices.

Published under license by AIP Publishing. https://doi.org/10.1063/1.5142649

Whispering gallery mode (WGM) microresonators<sup>1-4</sup> with an ultrahigh quality factor (Q) and a small mode volume, which could strongly enhance light-matter interaction, are suitable for both fundamental physics and photonic applications such as sensing, 5-14 lasing, 15-22 nonlinear optics, 23-27 optomechanics, 28-30 cavity quantum electrodynamics, 31,32 and non-Hermitian optics. 33-37 Particularly, a series of optical and thermal nonlinear effects can occur inside the cavity at relatively low input power due to significantly enhanced light intensities by resonance effects.<sup>38–47</sup> Thermal nonlinear oscillatory phenomena, such as regenerative pulsation at low temperature, 48 oscillatory instability resulting from thermal nonlinearity,39 and dynamic thermal behavior,<sup>38</sup> have been demonstrated in high-Q pure silica microresonators. Typically, they originate from the interplay between the resonance shift and optically induced effects, such as the thermaloptic effect, thermal expansion, free carrier dispersion, and Kerr effect. 39,48-55 Recent studies based on hybrid microresonators have also shown various kinds of dynamics, such as (1) thermo-optomechanical oscillation in poly(methyl methacrylate) (PMMA)-coated silica microtoroids, <sup>56</sup> (2) optical instability and self-pulsing in silicon nitride microresonators,50, <sup>4</sup> and (3) thermal oscillation in polydimethylsiloxane (PDMS)-coated microresonators. 51,52 In particular, optothermal mechanic effects enabled by thermal expansion of cavity materials have been demonstrated in PMMA-coated microtoroids<sup>56</sup> and ZBLAN microspheres.<sup>57</sup> Such effects combine the mechanical properties of optical material with the field intensity enhancement in resonators and, thus, can potentially be applied to build photothermal actuators with lower power consumption and fast actuation.

Natural structural proteins like bombyx mori silk fibroin are known for their robust mechanical properties, simple control of material properties through adjusting the water content during processing, programmable degradation, high transparency in the visible light band (>95%), and unique optical and electronic properties. <sup>59</sup> Consequently, silk-based optical devices are of great interest for in-vivo sensing applications. However, the rich nonlinearity enabled by the interaction between mechanical and optical properties of silk-based photonic structures remains largely unexplored.

Here, we experimentally demonstrate optothermally induced mechanical oscillation in a silk fibroin-coated high-Q microsphere. This hybrid microsphere consists of a silica core and a silk fibroin nanolayer coating. Theoretical analysis reveals that the observed oscillation results from the interplay among the positive thermo-optic effect of silica, negative thermo-optic effect, negative thermal expansion effect of silk fibroin, and dynamic thermal processes due to different thermal relaxation times in different regions of the structure. This oscillatory behavior is also found to be dependent on the optical input power. In contrast to previously studied hybrid microresonators such as the optothermal oscillation in PDMS-coated microtoroids, <sup>51</sup> the silk fibroin coating boosts the optothermo-mechanical (expansion) effect and results in this unique oscillatory waveform when coupled with the thermo-optical effect and the fast and slow thermal dynamic processes at different timescales.

The fabrication processes of the optical microresonator are presented as follows. Reconstituted silk solution was prepared as described in the previous literature.  $^{60}$  The process started with 2.5 g of

bombyx mori silkworm cocoons, which were cut into small pieces and then boiled in  $0.02 \mathrm{M}$  Na $_2\mathrm{CO}_3$  solution to remove sericin. The silk fiber was rinsed with cold ultrapure water for 20 min three times to ensure complete removal. The degummed silk was subsequently dried in a fume hood followed by a 4 h dissolution in 9.3M LiBr solution at  $60\,^{\circ}\mathrm{C}$ . Next, the dissolved silk solution was dialyzed against 1 L of ultrapure water using a Slide-a-Lyzer dialysis cassette (MWCO 3500, Thermo Fisher) for 48 h. The water was changed regularly six times during this period. The dialyzed silk solution was finally centrifuged twice at 9000 r.p.m at  $4\,^{\circ}\mathrm{C}$  for 20 min, resulting in 8 wt. % precursor silk solution. This precursor solution was then diluted 80-fold to 0.1 wt. % for the coating purpose.

A 50  $\mu$ m-diameter silica microsphere with a Q factor of  $10^8$  was first fabricated by melting a fiber tip with a  $CO_2$  laser. The dip coating technique was performed to coat the silk onto the microsphere controlled by a continuous motor. The sample was then exposed to 90% v/v methanol vapor at  $70\,^{\circ}$ C for 20 min to induce beta-sheet formation. The Q factor dropped to  $5\times10^6$  due to absorption loss in silk [Figs. 1(a) and 1(b)]. The fundamental WGM distribution of the coated microsphere resonator with a 60 nm-thick silk layer simulated by COMSOL reveals that 0.74% of the optical power circulates within the silk layer [Fig. 1(c)]. A silica wafer was coated with the same solution to characterize the coating by using an environmental SEM (Thermofisher Quattro S) and an ellipsometer (J.A. Woollam  $\alpha$ -SE). The silk film was confirmed, and the thickness was, thus, measured.

A tunable laser in the 1450 nm band was used to excite the hybrid microsphere through a taper fiber. The transmitted light signal was

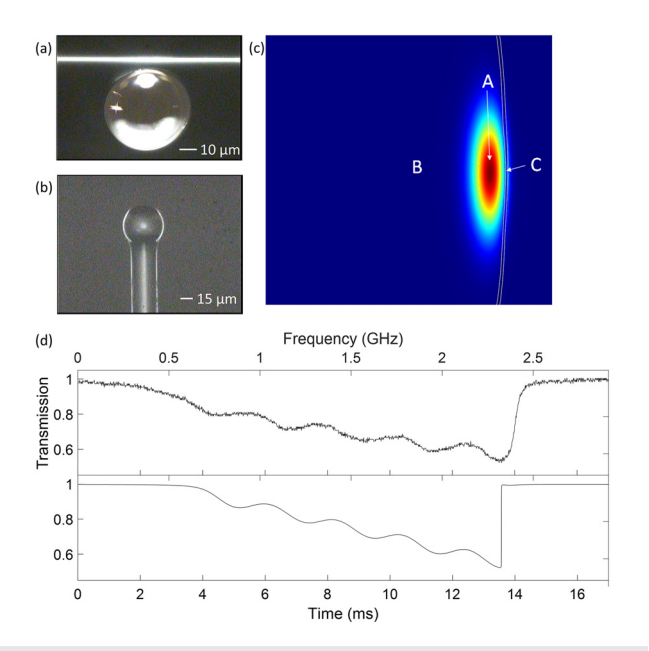


**FIG. 1.** Top (a) and side view (b) of a silk-coated microsphere coupled with a fiber taper under an optical microscope. The diameter of the microsphere was measured to be  $50~\mu m$ . (c) COMSOL simulation results showing mode distribution inside the microresonator: 98.23% in silica, 0.7% in silk, and 1.07% in air. (d) Experimental (top) and simulation (bottom) results of the transmission spectrum at an input power of 2.48 mW. The Q factor of the selected mode is  $5\times 10^6$ . The oscillation frequency of the experimental results was measured to be 437.07 Hz, while that of the simulated results was measured to be 467.34 Hz.

detected using a photoreceiver and monitored by an oscilloscope. A triangle wave was applied to the laser to implement a fine scan of the laser wavelength around the WGMs. When the scanning laser wavelength approached the cavity resonance wavelength, the transmission began to drop linearly with time [Fig. 1(d)]. At high input power, the oscillation line shape showed small amplitude changes along the downward side of the thermal triangle.

The self-oscillation phenomenon is generally found in resonant systems that involve opposite nonlinear mechanisms or two nonlinear processes with different scales of relaxation time. The oscillation in our system is not only attributed to the opposite thermo-optic and thermo-expansion effects in silica and silk fibroin but also owing to the different thermal relaxation times for different regions of the structure. It is worth noting that here for thermal expansion, the mechanical deformation is induced by the temperature change in silica and silk layers. The temperature oscillates due to competing thermo-optic effects in two layers and then drives the mechanical displacement to oscillate. The oscillation frequency is determined by the thermal oscillation rate instead of the mechanical resonant frequency.

We present a theoretical model to explain the physics behind the thermo-optomechanical oscillation. The effective refractive index of the WGM is described as  $n_{\it eff}\cong \eta_1 n_1 + \eta_2 n_2 + \eta_3 n_0$ , where  $n_1 = 1.45$ ,  $n_2 = 1.55$ , and  $n_0 = 1$  represent the refractive indices of silica, silk fibroin, and air, respectively;  $\eta_1$ ,  $\eta_2$ , and  $\eta_3$  represent the fraction of light traveling in the core, coating layer, and air, respectively, as  $\eta_1 + \eta_2 + \eta_3 = 1$ . In a hybrid microresonator, the time dependence of the temperature change varies as the respective thermal properties are different. In general, we need to consider two kinds of thermal processes: (1) the fast thermal relaxation from the mode volume to the rest of the cavity and (2) the slow thermal relaxation from the rest of the cavity to the ambient environment. While most previous works focused on only one type of those, our work shows the unique phenomenon caused by both. We divide our structure into three regions with different temperatures [Fig. 1(c)]: (A) the mode volume in the silica, (B) the rest of the silica without WGM, and (C) the mode volume in the silk layer. As a result, we consider several thermal transition processes in this system: (1) a fast thermal relaxation from the silica mode volume (region A) to the rest of the silica (region B), (2) a slow thermal relaxation from the non-mode volume of silica (region B) to the fiber stem, and (3) another slow thermal relaxation from the silk layer (region C) to the air (dominated by convection). The thermal conduction between silica and silk layer is much smaller than (1) and (3) and is, thus, neglected. We represent the temperature difference between regions A and B as  $\Delta T_{1a}$ , that between region B and the environment as  $\Delta T_{1b}$ , and that between region C and the environment as  $\Delta T_2$ . The diameter of the core  $d_1(t)$  and the thickness of the coating  $d_2(t)$  also vary as a result of thermal expansion. The resonant wavelength  $\lambda_r(t)$  of the WGM is written as

$$\begin{split} \lambda_r(t) &= \lambda_0 \left( 1 + \frac{\eta_1 \frac{dn_1}{dT} \Delta T_1(t) + \eta_2 \frac{dn_2}{dT} \Delta T_2(t)}{n_{eff}} \right. \\ &+ \frac{d_1(t)}{d_1(t) + 2d_2(t)} \frac{dL_1}{L_1 dT} \Delta T_1(t) d_1(t) \\ &+ \frac{2d_2(t)}{d_1(t) + 2d_2(t)} \frac{dL_2}{L_2 dT} \Delta T_2(t) d_2(t) + \frac{n_{kerr}}{n_{eff}} \frac{P_c(t)}{A} \right), \quad (1) \end{split}$$

where  $\lambda_0$  is the cold cavity resonance wavelength;  $\Delta T_1 = \Delta T_{1a} + \Delta T_{1b}$ is the temperature difference between region A and the environment;  $\frac{dn_1}{dT} = 1.2 \times 10^{-5} K^{-1}$  and  $\frac{dn_2}{dT} = -2.4 \times 10^{-4} K^{-1}$  designate the thermo-optic coefficients of silica and silk fibroin, respectively;  $\frac{dL_1}{L_1dT} = 5.5 \times 10^{-7} K^{-1}$  and  $\frac{dL_2}{L_2dT} = -2.4 \times 10^{-4} K^{-1}$  represent the linear thermal expansion coefficients of silica and silk fibroin, respectively; 51,62 n<sub>kerr</sub> represents the optical Kerr coefficient of silk fibroin; A is the effective cross-sectional area of the WGM; and  $P_c(t) = \frac{\left|E_C(t)\right|^2}{\tau}$ stands for the power of the intracavity field  $E_C(t)$ , where  $\tau_r = n_{eff} \pi (d_1 + 2d_2)/c$  represents the cavity round trip time.

The temperature changes within and outside of the mode volume can be expressed with the rate equations as follows:<sup>3</sup>

$$\frac{d\Delta T_{1a}(t)}{dt} = -\gamma_{th,1}\Delta T_{1a} + \gamma_{abs,1}P_c(t), \tag{2}$$

$$\frac{d\Delta T_{1a}(t)}{dt} = -\gamma_{th,1}\Delta T_{1a} + \gamma_{abs,1}P_c(t), \qquad (2)$$

$$\frac{d\Delta T_{1b}(t)}{dt} = -K_1\Delta T_{1b} + K_2\Delta T_{1a}, \qquad (3)$$

$$\frac{d\Delta T_2(t)}{dt} = -\gamma_{th,2}\Delta T_2 + \gamma_{abs,2}P_c(t),\tag{4}$$

where  $\gamma_{th,i}$  depicts the thermal relaxation rate and  $\gamma_{abs,i}$  describes the thermal absorption coefficient (i = 1: Silica, i = 2: Silk). Their values are obtained by curve fitting the experimental results:  $\gamma_{th,1} = 7.2 \times 10^4$  Hz,  $\gamma_{th,2} = 1568$  Hz,  $\gamma_{abs,1} = 697.7$  K/J, and  $\gamma_{abs,2}$ = 600.3 K/J. Here,  $K_1 = 1258 \,\mathrm{Hz}$  represents the thermal conductivity between (b) and the surrounding, while  $K_2 = 23918$  Hz is the thermal conductivity between (a) and (b), the values of which are obtained by fitting. The next rate equation describes the dynamics of the intracavity field,6

$$\frac{dE_c(t)}{dt} = (i\Delta\omega - \delta_0 - \delta_c)E_c(t) - \frac{\sqrt{2\delta_c}E_{in}}{\sqrt{\tau_r}},$$
 (5)

where  $\delta_0 = \omega_r/2Q_0$  denotes the intrinsic loss rate of the cavity, with  $Q_0$  being the intrinsic Q of the cavity, and  $\delta_c = \omega_r/2Q_c$  denotes the taper-cavity coupling induced loss rate, with  $Q_c$  representing the coupling Q.  $\Delta\omega(t) \equiv \omega_s(t) - \omega_r(t)$  is the detuning between the pump frequency  $\omega_s(t)$  and the resonance frequency  $\omega_r(t)$ . The excitation field  $E_{in}$  is related to the input power as  $|E_{in}|^2 = P_{in}\tau_r$ . Equation (5) is calculated using the Runge-Kutta (fourth order) method to obtain the intracavity field value. The field output is written as

$$E_o(t) = E_{in}(t) + \sqrt{\frac{2\delta_c}{\tau_r}} E_c(t). \tag{6}$$

The normalized transmission is calculated as  $T = |E_o(t)|^2/|E_{in}|^2$ .

Using the above theoretical model, we obtain a simulated transmission spectrum [Fig. 1(d)], which is in good agreement with the experimental result. To offer a physical interpretation of this oscillation, we simulate the time functions of temperature and diameter changes of the individual layers, the resonance wavelength, and the intracavity field (Fig. 2). There are two key mechanisms contributing to the overall oscillation: first, the thermal relaxation of silk fibroin is faster than that of the silica structure as a whole; second, the fast thermal relaxation from regions A to B resembles an effective Kerr effect that quickly responds to intracavity field changes. To study the latter, we consider the steady-state solution to Eq. (2), i.e.,

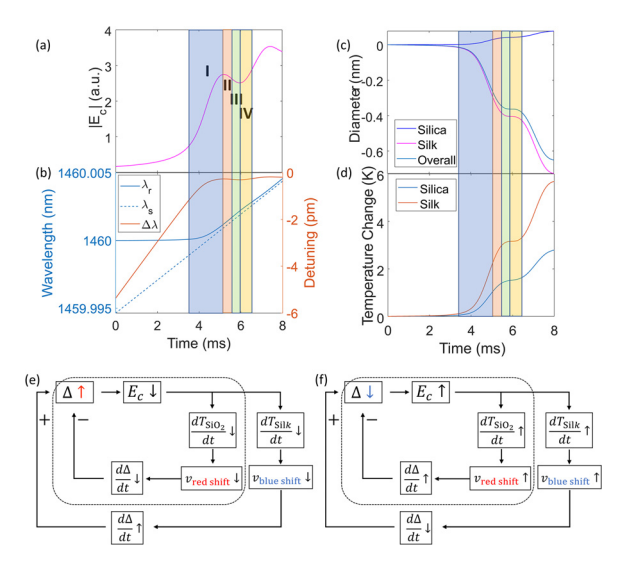


FIG. 2. Enlarged view of the first oscillation cycle of the simulated time-dependent variation of intracavity field E<sub>c</sub> (a), wavelength (detuning wavelength  $\Delta \lambda = \lambda_s - \lambda_r$ , where  $\lambda_s$  is the pump wavelength) (b), diameter change of the silica and silk layers (c), and temperature change in silica and silk (d) divided into four regions (I, II, III, and IV). Different color blocks mark the partition of each phase during one oscillation cycle. The feedback loops describe the dynamics in different regions. The dotted line circled region describes the stable negative feedback loop in a silica-only situation. (e) shows dynamics of regions II and III.  $\Delta$  represents the detuning between the pump and resonance frequencies. Increasing detuning leads to the decrease in the intracavity field, which, in turn, results in the decrease in the speed of temperature rise in both layers. The decreasing temperature rise in the silica core slows down the red shift in the resonance, thus slowing down the detuning rise, which composes a negative feedback loop. The decreasing temperature rise in the silk layer slows down the blue shift in the resonance, thus accelerating the detuning rise, which forms a positive feedback loop. (f) shows dynamics in regions I and IV, where the opposite process occurs.

$$\Delta T_{1a}(t) = \frac{\gamma_{abs,1} P_c(t)}{\gamma_{th,1}},\tag{7}$$

and the modified Eq. (1) becomes

$$\lambda_{r}(t) = \lambda_{0} \left( 1 + \frac{\eta_{1} \frac{dn_{1}}{dT} \Delta T_{1b}(t) + \eta_{2} \frac{dn_{2}}{dT} \Delta T_{2}(t)}{n_{eff}} + \frac{d_{1}(t)}{d_{1}(t) + 2d_{2}(t)} \frac{dL_{1}}{L_{1}dT} \Delta T_{1}(t) d_{1}(t) + \frac{2d_{2}(t)}{d_{1}(t) + 2d_{2}(t)} \frac{dL_{2}}{L_{2}dT} \Delta T_{2}(t) d_{2}(t) + \frac{\eta_{1} \frac{dn_{1}}{dT} \gamma_{abs,1} P_{c}(t)}{n_{eff} \gamma_{th,1}} + \frac{n_{kerr}}{n_{eff}} \frac{P_{c}(t)}{A} \right),$$
(8)

from which we can see that the term involving  $\Delta T_{1a}$  becomes equivalent to a Kerr-like term. Since this term is much larger than the intrinsic Kerr effect in silk and silica, we neglect the last term in Eq. (8).

To explain the dynamics of the thermo-opto mechanical oscillation in detail, we analyze the behavior depicted in Fig. 1(d) and Figs. 2(a)-2(d) section by section. When the scanning pump approaches the resonance wavelength, the intracavity field becomes stronger, causing a temperature increase in both silica and silk layers [Fig. 2(f)]. The positive optothermal effect of silica results in a red shift of resonance, whereas the negative optothermal and thermal expansion effects of silk result in a blue shift. As the positive effect outweighs the negative side, the resonance wavelength undergoes a red shift. However, since the silk layer undergoes a faster temperature rise than silica as a whole, the speed of this red shift starts off slow until SiO2 is fully heated. The red shift is then accelerated so that at the end of phase I, the speed of the red shift catches up with that of the scanning wavelength. The feedback loop shown in Fig. 2(e) describes phases II and III collectively. As the system enters phase II, the resonance red shift starts moving faster than the scanning wavelength, thus becoming further away from the pump. This causes the intracavity field to decrease, while the temperature rise continues as the system has yet to detect a significant change in the field. Thus, the red shift continues to accelerate. At the end of phase II, the acceleration of the red shift falls to zero as the speed reaches the maximum. However, as field intensity decreases, the fast optothermal effect in silica is reduced immediately. As a result, the resonance red shift slows down in phase III. At the end of this phase, the detuning reaches the maximum, the speed of the resonance red shift equates that of the scanning wavelength again, and the fast positive optothermal effect reaches its minimum point. Meanwhile, the temperature starts to react to the decaying field and, thus, decreases. Note that the temperature of the silk fibroin drops faster than that of silica as a whole. Starting from phase IV, the resonance red shift further slows down and becomes slower than that of the scanning wavelength. This reduces the detuning and, thus, increases the field [Fig. 2(f)]. The temperature of the silk layer reaches a low point and then gradually climbs up, which further slows down the red shift. Going into phase I of the next cycle, the temperature of silica finally catches up, thus driving the system forward with the next cycle coming, and so on and so forth. When the pump frequency finally catches up with the resonance frequency, the intracavity field reaches its maximum, after which the temperature falls so that the pump and resonance frequencies move in opposite directions, leading to a quick recovery of the transmission to one.

To understand the dependence of the optothermal oscillatory behavior on the field power, we first analyze the effect of varying input power on the oscillatory behavior (Fig. 3). For a small input power of 0.89 mW [Fig. 3(a)], the transmission spectrum shows a cavity Lorentzian line shape broadened by the positive optothermal effect. At the threshold condition, the falling edge of the triangle starts to oscillate like a wave [Fig. 3(b)]. As the input power increases, the downward edge widens, and more oscillating dips are observed [Figs. 3(c)-3(e)]. This is due to the fact that the resonance is easily caught up by the scanning pump wavelength at low input power; higher input power induces a larger temperature rise in the cavity, supporting a quicker and larger red shift so that the resonance is ahead of the pump wavelength for a longer period of time, allowing oscillation cycles to repeat. This observation, in general, agrees with our simulation results [Figs. 3(f)-3(j)]. The small discrepancy may owe to the fact that the distinct separation in our model between the environment and the non-mode volume silica is relatively gradual in reality.

In summary, we have theoretically and experimentally demonstrated the optothermal mechanical nonlinear oscillatory behavior in a

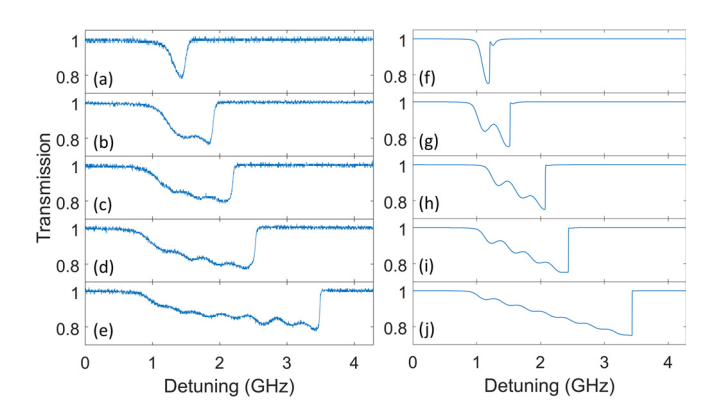


**FIG. 3.** Study of the oscillatory behavior with different input power. (a)–(e) Experimental transmission spectra with increasing input power, from a deformed Lorentzian shape to oscillation. The input power from top to bottom: 0.89 mW, 1.65 mW, 2.13 mW, 2.77 mW, and 3.40 mW. (f)–(j) The simulation results corresponding to the experimental results in (a)–(e).

high-Q silk fibroin-coated silica microsphere. The phenomenon is attributed to the thermal dynamic processes with different time scales as well as the combined interaction of several thermal nonlinear effects of the hybrid silk-coated-microsphere. Particularly, the input power is demonstrated to drastically change the oscillation behavior in the transmission spectra. We envision that this work will provide a platform for photothermal actuation with low power consumption, fast response, low cost, and biocompatibility. It will also open up further possibilities for the investigations of optical modulation, all-optical switching, and optical sensing by utilizing hybrid microresonators integrated with materials with a large thermal expansion coefficient.

This work was supported by NSF Grant No. ECCS1711451 and ARO Grant No. W911NF1710189.

## **DATA AVAILABILITY**

The data that support the findings of this study are available from the corresponding author upon reasonable request.

### **REFERENCES**

<sup>1</sup>K. J. Vahala, Nature **424**, 839 (2003).

<sup>2</sup>G. C. Righini, Y. Dumeige, P. Féron, M. Ferrari, G. N. Conti, D. Ristic, and S. Soria, Riv. Nuevo Cimento 34, 435 (2011).

<sup>3</sup>A. Chiasera, Y. Dumeige, P. Féron, M. Ferrari, Y. Jestin, G. Nunzi Conti, S. Pelli, S. Soria, and G. C. Righini, Laser Photonics Rev. 4, 457 (2010).

<sup>4</sup>X. Jiang, L. Shao, S.-X. Zhang, X. Yi, J. Wiersig, L. Wang, Q. Gong, M. Lončar, L. Yang, and Y.-F. Xiao, Science 358, 344 (2017).

<sup>5</sup>M. R. Foreman, J. D. Swaim, and F. Vollmer, Adv. Opt. Photonics 7, 168 (2015).

<sup>6</sup>F. Vollmer and S. Arnold, Nat. Methods 5, 591 (2008).

<sup>7</sup>L. Yang, X. Jiang, and A. J. Qavi, Proc. SPIE **10629**, 106290R (2018).

<sup>8</sup>F. Vollmer, L. Yang, and S. Fainman, Nanophotonics 1, 267 (2012).

X. Jiang, A. J. Qavi, S. H. Huang, and L. Yang, arXiv:1805.00062 (2018).
 S. H. Huang, S. Sheth, E. Jain, X. Jiang, S. P. Zustiak, and L. Yang, Opt. Express 26, 51 (2018).

<sup>11</sup>F. Shu, X. Jiang, G. Zhao, and L. Yang, Nanophotonics 7, 1455 (2018).

<sup>12</sup>L. Shao, X. F. Jiang, X. C. Yu, B. B. Li, W. R. Clements, F. Vollmer, W. Wang, Y. F. Xiao, and Q. Gong, Adv. Mater. 25, 5616 (2013).

<sup>13</sup>X. Xu, X. Jiang, G. Zhao, and L. Yang, Opt. Express 24, 25905 (2016).

- <sup>14</sup>J. Zhu, G. Zhao, I. Savukov, and L. Yang, Sci. Rep. 7, 1 (2017).
- <sup>15</sup>L. He, ŞK. Özdemir, and L. Yang, Laser Photonics Rev. 7, 60 (2013).
- <sup>16</sup>X.-F. Jiang, Y.-F. Xiao, C.-L. Zou, L. He, C.-H. Dong, B.-B. Li, Y. Li, F.-W. Sun, L. Yang, and Q. Gong, Adv. Mater. 24, OP260 (2012).
- 17X.-F. Jiang, C.-L. Zou, L. Wang, Q. Gong, and Y.-F. Xiao, Laser Photonics Rev. 10, 40 (2016)
- <sup>18</sup>G. Zhao, ŞK. Özdemir, T. Wang, L. Xu, E. King, G. L. Long, and L. Yang, Sci. Bull. **62**, 875 (2017).
- <sup>19</sup>G. Lin, S. Diallo, K. Saleh, R. Martinenghi, J. C. Beugnot, T. Sylvestre, and Y. K. Chembo, Appl. Phys. Lett. **105**, 231103 (2014).
- <sup>20</sup>X. F. Jiang, Y. F. Xiao, Q. F. Yang, L. Shao, W. R. Clements, and Q. Gong, Appl. Phys. Lett. **103**, 101102 (2013).
- <sup>21</sup>L. Yang, T. Carmon, B. Min, S. M. Spillane, and K. J. Vahala, Appl. Phys. Lett. 86, 091114 (2005).
- <sup>22</sup>L. Yang, D. K. Armani, and K. J. Vahala, Appl. Phys. Lett. **83**, 825 (2003).
- <sup>23</sup>Y. Li, X. Jiang, G. Zhao, and L. Yang, arXiv:1809.04878 (2018).
- <sup>24</sup>J. Topolancik and F. Vollmer, Appl. Phys. Lett. 89, 184103 (2006).
- 25G. Lin, J. U. Fürst, D. V. Strekalov, and N. Yu, Appl. Phys. Lett. 103, 181107 (2013).
- <sup>26</sup>C. Z. Chai, X. X. Hu, C. L. Zou, G. C. Guo, and C. H. Dong, Appl. Phys. Lett. 114, 021101 (2019).
- <sup>27</sup>H. S. Choi and A. M. Armani, Appl. Phys. Lett. **97**, 223306 (2010).
- <sup>28</sup>M. Aspelmeyer, T. J. Kippenberg, and F. Marquardt, Rev. Mod. Phys. 86, 1391 (2014).
- <sup>29</sup>j. D. Thompson, B. M. Zwickl, A. M. Jayich, F. Marquardt, S. M. Girvin, and J. G. E. Harris, Nature 452, 72 (2008).
- <sup>30</sup>X. Jiang, M. Wang, M. C. Kuzyk, T. Oo, G.-L. Long, and H. Wang, Opt. Express 23, 27260 (2015).
- <sup>31</sup>H. Mabuchi and A. C. Doherty, Science **298**, 1372 (2002).
- <sup>32</sup>D. V. Strekalov, C. Marquardt, A. B. Matsko, H. G. L. Schwefel, and G. Leuchs, J. Opt. 18, 123002 (2016).
- 33W. Chen, ŞK. Özdemir, G. Zhao, J. Wiersig, and L. Yang, Nature 548, 192 (2017).
- <sup>34</sup>R. El-Ganainy, K. G. Makris, M. Khajavikhan, Z. H. Musslimani, S. Rotter, and D. N. Christodoulides, Nat. Phys. 14, 11 (2018).
- 35K. Özdemir, S. Rotter, F. Nori, and L. Yang, Nat. Mater. 18, 783 (2019).
- <sup>36</sup>B. Peng, S. K. Özdemir, F. Lei, F. Monifi, M. Gianfreda, G. L. Long, S. Fan, F. Nori, C. M. Bender, and L. Yang, Nat. Phys. 10, 394 (2014).
- <sup>37</sup>C. Wang, X. Jiang, G. Zhao, M. Zhang, C. W. Hsu, B. Peng, A. D. Stone, L. Jiang, and L. Yang, Nat. Phys. 16, 334 (2020).
- 38T. Carmon, L. Yang, and K. J. Vahala, Opt. Express 12, 4742 (2004).
- <sup>39</sup>V. S. Il'chenko and M. L. Gorodetskii, Laser Phys. 2, 1004 (1992).

- <sup>40</sup>E. Kim, M. R. Foreman, M. D. Baaske, and F. Vollmer, Appl. Phys. Lett. 106, 161101 (2015).
- <sup>41</sup>B.-B. Li, Q.-Y. Wang, Y.-F. Xiao, X.-F. Jiang, Y. Li, L. Xiao, and Q. Gong, Appl. Phys. Lett. **96**, 251109 (2010).
- <sup>42</sup>L. He, Y.-F. Xiao, C. Dong, J. Zhu, V. Gaddam, and L. Yang, Appl. Phys. Lett. 93, 201102 (2008).
- <sup>43</sup>C. H. Dong, L. He, Y. F. Xiao, V. R. Gaddam, S. K. Ozdemir, Z. F. Han, G. C. Guo, and L. Yang, Appl. Phys. Lett. **94**, 231119 (2009).
- 44W. Chen, J. Zhu, ŞK. Özdemir, B. Peng, and L. Yang, Appl. Phys. Lett. 109, 061103 (2016).
- 45J. Zhu, Ş. Kaya Özdemir, L. He, and L. Yang, Appl. Phys. Lett. 99, 171101
- 46 H. Rokhsari, S. M. Spillane, and K. J. Vahala, Appl. Phys. Lett. 85, 3029 (2004)
- 47 Y. Zhi and A. Meldrum, Appl. Phys. Lett. **105**, 031902 (2014).
- <sup>48</sup>Y.-S. Park and H. Wang, Opt. Lett. **32**, 3104 (2007).
- <sup>49</sup>T. J. Johnson, M. Borselli, and O. Painter, Opt. Express 14, 817 (2006).
- <sup>50</sup>C. Baker, S. Stapfner, D. Parrain, S. Ducci, G. Leo, E. M. Weig, and I. Favero, Opt. Express 20, 29076 (2012).
- <sup>51</sup>L. He, Y.-F. Xiao, J. Zhu, S. K. Ozdemir, and L. Yang, Opt. Express 17, 9571 (2009)
- 52Z.-C. Luo, C.-Y. Ma, B.-B. Li, and Y.-F. Xiao, AIP Adv. 4, 122902 (2014).
- 53S. Diallo, G. Lin, and Y. K. Chembo, Opt. Lett. 40, 3834 (2015).
- <sup>54</sup>J. Wang, B. Zhu, Z. Hao, F. Bo, X. Wang, F. Gao, Y. Li, G. Zhang, and J. Xu, Opt. Express 24, 21869 (2016).
- 55 X. Sun, H. Liang, R. Luo, W. C. Jiang, X.-C. Zhang, and Q. Lin, Opt. Express 25, 13504 (2017).
- 56Y. Deng, F. Liu, Z. C. Leseman, and M. Hossein-Zadeh, Opt. Express 21, 4653 (2013).
- 57Y. Deng, M. R. Flores-Flores, R. K. Jain, and M. Hossein-Zadeh, Opt. Lett. 38, 4413 (2013).
- 58T. Wang, D. Torres, F. E. Fernández, C. Wang, and N. Sepúlveda, Sci. Adv. 3, e1602697 (2017).
- <sup>59</sup>H. Tao, D. L. Kaplan, and F. G. Omenetto, Adv. Mater. **24**, 2824 (2012).
- <sup>60</sup>D. N. Rockwood, R. C. Preda, T. Yücel, X. Wang, M. L. Lovett, and D. L. Kaplan, Nat. Protoc. 6, 1612 (2011).
- <sup>61</sup>X. Jiang and L. Yang, Light Sci. Appl. **9**, 24 (2020).
- <sup>62</sup>L. Xu, X. Jiang, G. Zhao, D. Ma, H. Tao, Z. Liu, F. G. Omenetto, and L. Yang, Opt. Express 24, 20825 (2016).
- <sup>63</sup> A. E. Fomin, M. L. Gorodetsky, I. S. Grudinin, and V. S. Ilchenko, J. Opt. Soc. Am. B 22, 459 (2005).
- 64M. L. Gorodetsky and V. S. Ilchenko, J. Opt. Soc. Am. B 16, 147 (1999).